Proof-of-principle experiment for the dark-field detection concept for measuring vacuum birefringence

Michal Šmíd,[1,*] Pooyan Khademi,[2,3,4] Naser Ahmadiniaz,[1] Michal Andrzejewski,[5] Carsten Baehtz,[1] Erik Brambrink,[5] Jakub Bulička,[6,7] Tomáš Burian,[6] Samuele Di Dio Cafiso,[1] Jaromír Chalupský,[6] Thomas E. Cowan,[1,8] Sebastian Göde,[5] Jörg Grenzer,[1] Věra Hájková,[6] Peter Hilz,[2,3,4] Willi Hippler,[2,3,4] Hauke Höppner,[1] Alžběta Horynová,[6,9] Lingen Huang,[1] Oliver Humphries,[5] Šimon Jelínek,[10,6,7] Libor Juha,[6] Felix Karbstein,[2,3,4,†] Christian Kohlfürst,[1] Alejandro Laso Garcia,[1] Robert Lötzsch,[2,3,4] Masruri Masruri,[5] Aimé Matheron,[2,3,4] Motoaki Nakatsutsumi,[5] Gerhard G. Paulus,[2,3,4] Alexander Pelka,[5] Thomas R. Preston,[5] Sripati V. Rahul,[5] Lisa Randolph,[5] Alexander Sävert,[2,3,4] Hans-Peter Schlenvoigt,[1] Ralf Schützhold,[1,8] Jan Patrick Schwinkendorf,[1,5] Thomas Stöhlker,[2,3,4] Monika Toncian,[1] Toma Toncian,[1] Maksim Valialshchikov,[2,3,4] Vojtěch Vozda,[6] Edgar Weckert,[11] Colin Wessel,[2,3,4] Jan Wild,[7] Ulf Zastrau,[5] and Matt Zepf[2,3,4,‡]

[1]*Helmholtz-Zentrum Dresden-Rossendorf, Bautzner Landstraße 400, 01328 Dresden, Germany*
[2]*Helmholtz-Institut Jena, Fröbelstieg 3, 07743 Jena, Germany*
[3]*GSI Helmholtzzentrum für Schwerionenforschung, Planckstraße 1, 64291 Darmstadt, Germany*
[4]*Faculty of Physics and Astronomy, Friedrich-Schiller-Universität Jena, 07743 Jena, Germany*
[5]*European XFEL, Holzkoppel 4, 22869 Schenefeld, Germany*
[6]*Department of Radiation and Chemical Physics, Institute of Physics, Czech Academy of Sciences, Na Slovance 2, 182 00 Prague 8, Czech Republic*
[7]*Department of Surface and Plasma Science, Faculty of Mathematics and Physics, Charles University, V Holešovičkách 2, 182 00 Prague 8, Czech Republic*
[8]*Technische Universität Dresden, 01062 Dresden, Germany*
[9]*Department of Nuclear Chemistry, Faculty of Nuclear Science and Physical Engineering, Czech Technical University in Prague, Břehová 7, 115 19 Prague 1, Czech Republic*
[10]*Laser Plasma Department, Institute of Plasma Physics, Czech Academy of Sciences, Za Slovankou 3, 182 00 Prague 8, Czech Republic*
[11]*Deutsches Elektronen-Synchrotron DESY, Notkestrasse 85, 22607 Hamburg, Germany*

(Received 2 July 2025; accepted 10 November 2025; published 8 December 2025)

Vacuum fluctuations give rise to effective nonlinear interactions between electromagnetic fields. These generically modify the characteristics of light traversing a strong-field region. X-ray free-electron lasers (XFELs) constitute a particularly promising probe, due to their brilliance, the possibility of precise control and favorable frequency scaling. However, the nonlinear vacuum response is very small even when probing a tightly focused high-intensity laser field with XFEL radiation and direct measurement of light-by-light scattering of real photons and the associated fundamental physics constants of the quantum vacuum has not been possible to date. Achieving a sufficiently good signal-to-background separation is key to a successful quantum vacuum experiment. To master this challenge, a dark-field detection concept has recently been proposed. Here we present the results of a proof-of-principle experiment validating this approach by demonstrating that using real-world x-ray optics the background signal can be suppressed sufficiently to measure the weak nonlinear response of the vacuum.

DOI: 10.1103/xpxy-ntwz

I. INTRODUCTION

The main challenge of experiments aiming at measuring the nonlinear response of the quantum vacuum to strong macroscopic electromagnetic fields is to discriminate the small signal component from the large background of the probe beam. For instance, when an -ray free-electron laser (XFEL) probe pulse comprising a large number $N \sim 10^{11}$ of photons with an energy of $\omega \sim 10\,\mathrm{keV}$ collides with a tightly focused Petawatt-class laser beam, the attainable quantum vacuum signals are typically below the single photon level per shot; cf. Ref. [1] and references therein. The signal induced in a mode polarized perpendicular to the linearly polarized probe is the signature of vacuum birefringence. The requirements for a successful measurement of the nonlinear vacuum response are a twofold: on the one hand the signal itself must be sufficiently large to be detected. On the other hand, the

*Contact author: m.smid@hzdr.de
†Contact author: f.karbstein@hi-jena.gsi.de
‡Contact author: m.zepf@hi-jena.gsi.de

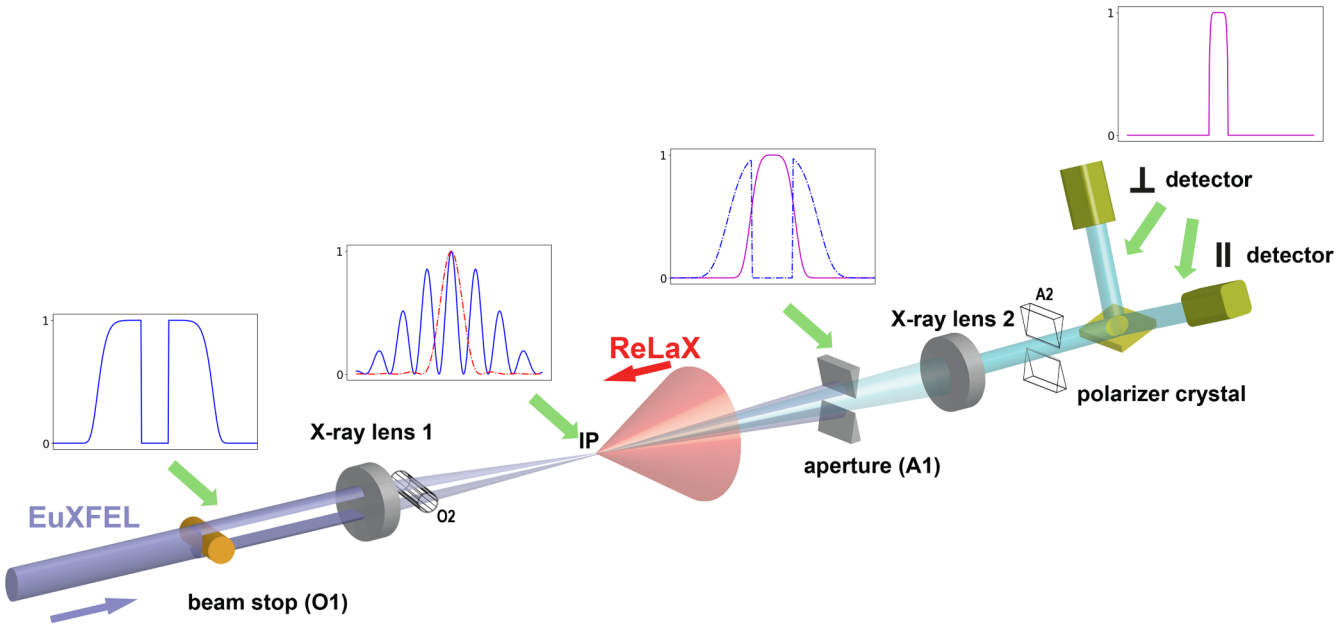

FIG. 1. Idealized dark-field setup with normalized intensity distributions at each critical plane indicated by a green arrow. The primary x-ray distributions (blue) are shown as for four planes with the dashed red line showing the laser focal intensity distribution. The central shadow is imprinted onto the x-ray probe beam by inserting an opaque beam stop ("obstacle"), transforming the initial distribution with a central maximum. In the focal plane a peaked distribution reappears with the shadow encoded in side lobes appearing in the focus. At the interaction point (IP) the central peak overlaps with the high-intensity laser (ReLaX) focus. For matched x-ray and laser waists the resulting quantum vacuum signal (magenta line in the aperture plane) is peaked on axis, due to the suppression of the side lobes in the interaction. An additional object O2 immediately after the first lens and matching aperture A2 in the image plane of O2 can also be introduced. In the experiment, the detectors are in the focus of lens 2.

background from the probe beam must be small enough so as not to mask the signal. Ideally the signal should be greater than the background to allow for a significant measurement within a realistic experimental duration. The experiment must therefore be designed to allow the signal photons to be distinguished from the background. In principle the response of the quantum vacuum can result in signals which differ from the probe beam in terms of their polarization, angular distribution and photon energy. Of particular interest are configurations, that allow the fundamental coupling parameters a and b governing the effective interaction of electromagnetic fields in the underlying theory ($c = \hbar = 1$) [2],

$$\mathcal{L}_{\rm int} \simeq \frac{m^4}{1440\pi^2}\left[a\left(\frac{\vec{B}^2-\vec{E}^2}{E_{\rm S}^2}\right)^2 + b\left(\frac{2\vec{B}\cdot\vec{E}}{E_{\rm S}^2}\right)^2\right], \quad (1)$$

to be determined and thus the theoretical framework to be tested in detail (m is the electron mass and $E_{\rm S} = m^2/e = 1.3\times10^{18}\,{\rm V/m}$ the *critical* electric field). Quantum electrodynamics (QED) predicts $a \simeq 4$ and $b \simeq 7$ [3,4]. Higher order corrections are parametrically suppressed by powers of the fine-structure constant $\alpha = 1/137$. The coupling parameters a and b are also sensitive to physics beyond the Standard Model because Eq. (1) generically emerges as the weak-field limit of theories respecting a charge conjugation parity symmetry. Both the parallel and perpendicularly polarized components must be measured to determine a and b. A prospective candidate is the dark-field concept [5–7] utilizing the angular distribution to separate the signal from the background. Here we consider the specific implementation put forward in Ref. [8] using an XFEL probe colliding with a tightly focused high-intensity pump. In the following, we detail this measurement concept and report the performance of a recent implementation at the High Energy Density (HED) scientific instrument of the European X-ray Free Electron Laser (EuXFEL) [9]. Finally, we review the requirements for successful measurement of vacuum birefringence in this setup.

II. DARK-FIELD MEASUREMENT CONCEPT

The idea underlying the dark-field (DF) concept is to choose an experimental setup, where the desired signal is contained in an angular range which is essentially free from any background, thereby maximizing the signal to background ratio $\mathcal{R}$.[1] In the specific case of the x-ray DF scenario devised for the measurement of the nonlinear quantum vacuum response, the probe beam is modified with a well-defined obstacle such as to exhibit a shadow in both the converging and expanding beam while retaining a peaked focus profile; see Fig. 1 for an illustration. Wave optics implies that in the focus the information about the shadow in the beam is encoded in pronounced side peaks. The number of x-ray signal photons $N_{\rm sig}$ induced in the collision with the high-intensity pump scales linearly (quadratically) with the intensity of the

[1]To our knowledge this is true in the context of two beam interactions. Multibeam geometries add further possibilities at the cost of added complexity.

probe (pump). In line with that, the product of the transverse focus profile of the probe and the squared pump focus profile determines the signal source distribution. Hence, the signal source distribution differs substantially from the probe focus profile and has a different angular distribution; see Fig. 1.

Appropriate tuning of the pump and probe waists allows the source distribution of the quantum vacuum signal to be modified; in particular the side lobes can be significantly reduced relative to central peak in the signal source distribution for sufficiently small pump foci. For a probe beam with a central shadow, these side lobes in its focus encode the shadow imprinted in its near field.

Effectively erasing the side lobes in the source distribution of the quantum vacuum signal ensures that the signal does not inherit any information about the shadow in the incident probe beam. Ideally, only the central near-Gaussian peak is left as signal source. This results in an angular signal distribution that is essentially Gaussian and resembles that of the unobstructed probe beam.

In summary, the above approach allows the maximum of the quantum vacuum signal to propagate into the minimum of the shadow in the probe beam, resulting in substantially improved signal to background ratio $\mathcal{R}$, thus facilitating the detection of the extremely weak quantum vacuum signals.

For sufficiently good background suppression in the shadow and reasonably strong quantum vacuum signals, the DF concept should even facilitate the detection of both the parallel ($\parallel$) and perpendicular ($\perp$) polarized components of the nonlinear vacuum response. This, in turn, would provide direct access to the low-energy constants a and b. The key parameter of the DF concept is therefore the quality of the shadow. The latter can be quantified in terms of the unwanted background measured within the shadow. For lossless beam transport we define the shadow factor associated with a detector of a given detection area A_{DET} (parametrized by the coordinates x and y) as

$$\mathcal{S} = \frac{1}{N} \int_{A_{\mathrm{DET}}} \mathrm{d}^2x \, \frac{\mathrm{d}^2N(x,y)}{\mathrm{d}x\,\mathrm{d}y}. \tag{2}$$

For a given detector, $\mathcal{S}$ is the ratio of photons indistinguishable from the quantum vacuum signal to the total number of photons N in the initial x-ray beam.

III. EXPERIMENTAL IMPLEMENTATION AND DESIGN CONSIDERATIONS

While the outcome of an elementary proof-of-concept experiment of the dark-field approach at an x-ray tube [8] and the results of numerical diffraction simulations [1] are promising, reliable information about the shadow factor achievable with an XFEL probe can be drawn only from a full-scale experiment. To validate the dark-field detection concept, a dedicated x-ray-only proof-of-concept experiment was carried out at the HED scientific instrument of the European XFEL in a beamtime granted by the Helmholtz International Beamline for Extreme Fields (HIBEF) priority access program. This ensures that the beam characteristics are those achievable in a combined experiment and allows a predictive simulation capability to be developed.

In a hypothetical arrangement with perfect imaging and no scattering, the DF would have zero background from the primary XFEL beam in the detector area defined by aperture A1 with the layout in Fig. 1.

In a real-world scenario, every scattering or diffraction event modifies the angular distribution of the x-rays and imaging properties. and the combination of two such events can result in a background x-ray photon propagating along the signal path. Therefore, it is clear that diffracted and scattered x-rays pose the main source of background that must be suppressed. Diffraction occurring around the obstacles (O1, O2) results in x-rays propagating at an angle to the unperturbed beam and, as a consequence of that, x-ray photons in the geometric shadow of the blocking obstacles. A single further scattering or diffraction event allows such photons to be deflected onto a path leading to the Region of Interest (ROI, typically a single detector pixel) on the detector plane in the focus of lens 2.

Diffraction is suppressed by imaging the obstacles on the matching aperture plane (i.e., O1 images to A1, O2 to A2, and interaction point pinhole to the detector plane). In the limit of perfect imaging, aperture sizes A1, A2 could be chosen to match the size of the obstacles, thus maximizing transmission of the quantum vacuum signal. In practice, image quality is limited by the small numerical aperture of the x-ray lenses (lens 1 and lens 2). The point spread function results in a less sharp obstacle edge, requiring smaller apertures to minimise background caused by diffraction from A1, A2. Typically, the apertures were set to a quarter of the size of the image of the obstacle.

Scattering in the beryllium compound refractive lenses (CRLs) [10] can also contribute background photons. The central area of the first lens, for example, is irradiated by photons diffracted into the geometrical shadow of obstacle O1. Those photons are then scattered among others onto the beam axis, going directly towards detector ROI. To prevent this, the obstacle O2 located just after the lens is introduced. The lens scattering outside of the obstacle shadow, on the other hand, is blocked by the pinhole positioned in the interaction point (IP) between optical and x-ray beams in the focal plane of lens 1. The diameter of the pinhole is chosen so that there is no direct line of sight between the brightly illuminated area of lens 1 and opening of A1. Scattering on lens 2 is controlled by making sure that no strong beam is reaching the lens, i.e., the direct part of beam is blocked by A2.

Unless further measures are taken, the scattering in the lens 1 will result in (a) scattering of the diffracted x-rays from O1 into the ROI and (b) homogeneous illumination of lens 2 by scattering from lens 1. In our setup, scenario (a) is blocked by O2, while scenario (b) is blocked by inserting a pinhole at the interaction point. The combination of O2 and pinhole prevents scattered photons from reaching the lens 2 when A1 is chosen to be smaller than the pinhole shadow.

In this arrangement a beam photon must be deviated at least *three* times through scattering or diffraction to reach the ROI.

IV. RESULTS

To determine the viability of the scheme on the HED Beamline at European XFEL an experiment to characterize

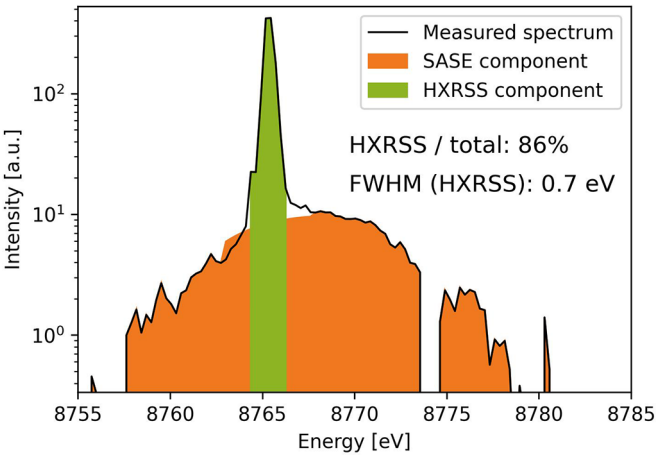

FIG. 2. XFEL spectrum measured by the HIREX spectrometer. The SASE bandwidth is 25 eV with seeded peak positioned at 8766 eV with FWHM 0.7 eV containing 86% of the beam energy.

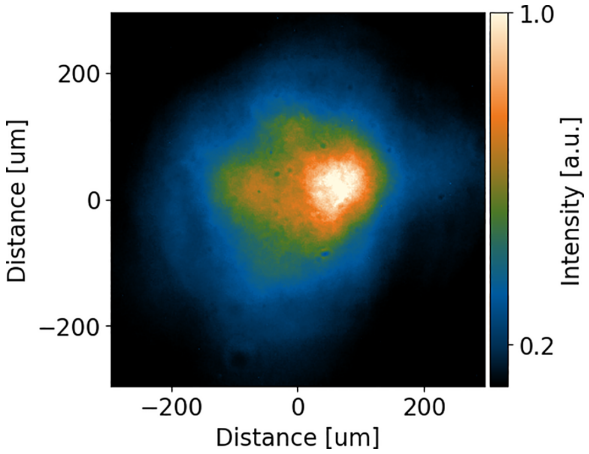

FIG. 3. Collimated XFEL beam profile on the detector plane.

the dark-field setup was performed. This experiment had three main aims. First, we characterize the XFEL properties critical for this kind of experiment. Special attention is put on the focus profile of the XFEL beams with and without obstacle inserted. Second, we get scattering data on used components to asses the material properties and guide the simulations to predictive capabilities. Lastly, we perform the complex setup, demonstrate its feasibility, and determine the shadow factor $\mathcal{S}$. This is particularly important, as scattering and diffraction depend in detail on microscale surface topology and (non-)uniformity of the bulk composition. Therefore the exact background in the ROI, and subsequently the overall viability of the experiment, can only be determined experimentally.

A. XFEL beam properties

The XFEL was operated in the hard x-ray self seeded mode (HXRSS) [11]. Compared to the SASE regime, this results in a reduction in total photon number while increasing the flux in a narrow (sub-eV) bandwidth. Narrow bandwidth is essential to achieve well-defined focal quality with minimal chromatic aberrations and to maximize the signal within the angular acceptance (and therefore reflection bandwidth) of the crystal polarizing optics used in the detection setup.

The EuXFEL delivered beam had pulse energies in the range of $W_x = 300$–$500\,\mu$J in seeded mode, as measured by gas monitors before entering the HED instrument beamline. Figure 2 shows the XFEL spectrum measured with the HIREX spectrometer [12]. The seeded peak (FWHM <1 eV) set at $\omega = 8766$ eV ($\lambda = 0.141$ nm) is clearly visible above the SASE background ($\approx$25 eV bandwidth). It contains 86% of the total pulse energy.

The XFEL beam shown in Fig. 3 was focused using a beryllium CRL with a focal length of $f = 438$ mm measured from the middle of the 13-element lens stack. Predicting the quantum vacuum signal in this setup requires detailed knowledge of the XFEL focus. This was characterized using specially designed and characterized ablation targets, consisting of highly damage-resistant diamond substrate with a well-defined PbI_2 coating serving as the ablation material [13,14]. Figure 4 shows the composite image of multiple ablation shots in the focal position. The analytic approximation of the focus intensity profile ("Airy focus")

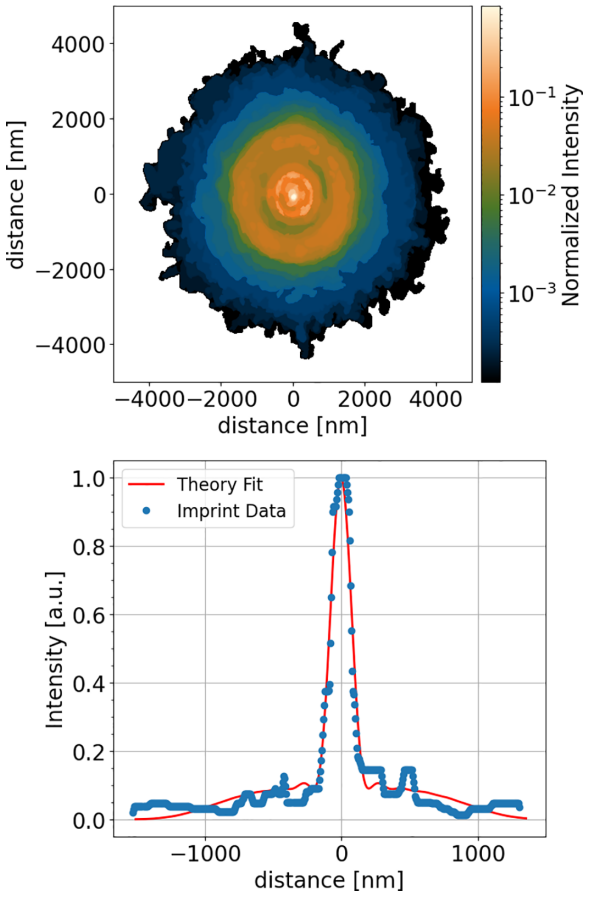

FIG. 4. Focal intensity distribution of the full XFEL beam measured with ablation imprints (top panel). The bottom panels shows a lineout through the center of the imprint (blue dots) and a theoretical fit (red line). The fit is an Airy focus with central peak diameter ($2w_0$) of 240 nm to which a small super-Gaussian background representing the scattering background in the focusing lenses is added; see main text.

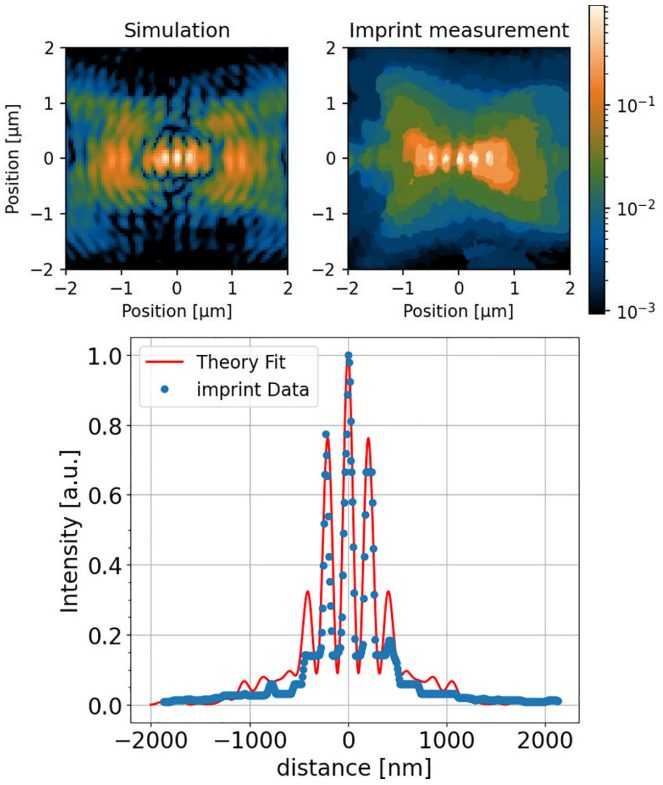

FIG. 5. Focal distribution of XFEL beam with 160 μm electrochemically polished tungsten wire as obstacle O1 and another as O2 after lens 1, simulation (top left panel), and reconstruction from the imprint measurement (top right). Both normalized. (lower panel) the central line out of the imprint measurements (blue dots), and the theoretical fit (red line) yielding an $1/e^2$ width ($2w_0$) of 180 nm for the central peak.

$I(r) = I_0[J_1(2\sqrt{2(1-e^{-1})}\, r/w_0)/(\sqrt{2(1-e^{-1})}\, r/w_0)]^2$ of a rotationally symmetric beam with a flat top transverse profile in its near field was fitted to the data. Here I_0 is the peak intensity, J_n is the Bessel function of the first kind of order n, and w_0 is the beam waist at approximate $1/e^2$ [15].

We emphasize that the goal here (and for the analogous considerations in Sec. IV B below) is not to demonstrate perfect agreement of the measured focus profiles with advanced beam models matching the precise experimental conditions, but rather to highlight the remarkable agreement with a vastly idealized analytical beam model. This convincingly illustrates the exceptional performance of the XFEL with regard to its beam properties and serves as an indication for the appropriateness of our analytical estimates for the attainable QED vacuum signals presented in Sec. V below.

The broad-band SASE background visible in Fig. 2 is focused at different positions along the focal axis due to lens chromaticity and adds a low-intensity pedestal at the focus of the seeded peak. The latter is fitted by a super-Gaussian function $\sim \exp[-1/2\,(r/\sigma)^4]$ with $\sigma = 850$ nm and peak intensity of about $I_0/10$ and is added to the Airy focus fit in Figs 4 and 5. The fit yields a width of the central peak ($2w_0$) of 240 nm (140 nm FWHM), demonstrating near-diffraction limited focusing. The diffraction-limited value is $2w_0 \simeq 2\lambda(f/d)\sqrt{8(1-e^{-1})}/\pi = 227$ nm [15]. The data shown in the following were recorded with an average XFEL beam energy of 108 μJ measured after lens 1; we obtain an effective photon number of $N_0 = 6.58 \times 10^{10}$ in the central Airy peak containing 68.8% at $I > I_0/e^2$ in this run. The photon number N_0 in the collimated beam without obstacle but corrected for lens losses is the input into our theoretical calculations of the expected quantum vacuum signal in Sec. V below.

B. Focal distribution with beam-stop object

As described above, the key steps to implementing the dark-field measurement setup are first to imprint a high-quality shadow in the EuXFEL beam and then to interact a tightly focused high-intensity laser with the x-ray far-field intensity pattern the lens focus, resulting in a quantum vacuum signal with a strong signal in the shadow. The central shadow was created using a polished tungsten wire with a diameter of 160 μm as obstacle (Fig. 1), obscuring about half of the beam (52.2% of the beam area).

The shadow of the wire results in fringes in the focus of the beam. The experimentally observed pattern with a periodicity of 0.2 μm is shown in Fig. 5. The analytic approximation of the focal intensity profile of a beam with flat top near-field profile (width d) featuring a central rectangular shadow (width $d_{\rm wire}$) is $I(x) = I_0 \cos^2(\frac{(1+\nu)f(\nu)}{2}\frac{x}{w_0})\,\mathrm{sinc}^2(\frac{(1-\nu)f(\nu)}{2}\frac{x}{w_0})$, where x is the coordinate perpendicular to the wire, $\nu = d_{\rm wire}/d$, and $f(\nu) = \sqrt{6(1-e^{-1})(1-\nu)/(1-\nu^3)}$ [16] This profile is fitted to the data and yielded a central peak diameter ($2w_0$) of 180 nm fitted at approximate $1/e^2$ compared to the data. The same super Gaussian function as for the case of the unobstructed XFEL beam is added to model the low-intensity SASE background. Small discrepancies between measured data and theory in the higher order (side) peaks are visible.

Importantly, the focus imprint measurements presented in Figs. 4 and 5 validate the key assumption of the dark-field concept, namely, the appropriateness of a coherent beam description for the XFEL beam. It is evident that, without this, the setup illustrated in Fig. 1 would not work.

C. Determination of shadow factor

The shadow factor $\mathcal{S}$ used in the theoretical considerations can be derived from the experimental ratio between the signal in the ROI containing the image of the focal spot with and without blocking object(s) in place, which we denote $\mathcal{S}_{\rm exp}$. The detector is placed in the image of the XFEL focus created by lens 2.

The experimental ratio $\mathcal{S}_{\rm exp}$ is related to the shadow factor $\mathcal{S}$ in Eq. (2) as $\mathcal{S} = T_{A1} \times \mathcal{S}_{\rm exp}$, with T_{A1} the transmission at the aperture A_1.

Figure 6 shows an image taken with a high-resolution scintillator camera at the image plane. By design, the most intense diffracted or scattered light is visible outside the image of the focus with the image of the focus restricted to one pixel in the center of the distribution. From the distribution of the signal in Fig. 6, it is clear that the background signal depends on the pixel size of the detector (Jungfrau: 75 μm, Andor iKon 13 μm). The image of the focus is typically smaller than the pixel size). Most scans were performed with the Jungfrau

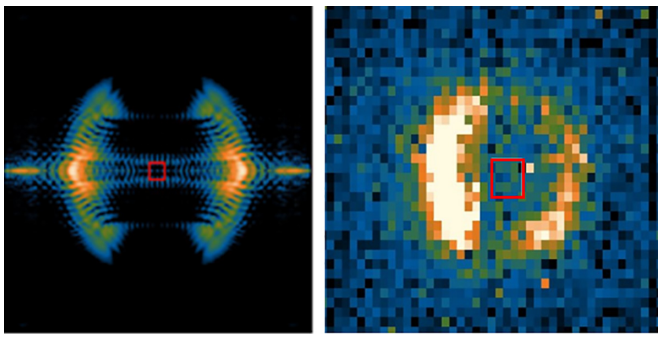

FIG. 6. Comparison of image on detector plane from simulations (left) and experiment with high-resolution scintillator (right). The bright feature is scattering from the 25 μm tungsten pinhole illuminated by scattered and diffracted x-rays. The red square is 13 μm ROI.

detector [17], due to its single-photon sensitivity, large dynamic range, and fast acquisition. Figure 7 shows $\mathcal{S}$ as a function of the aperture sizes A_1, A_2 for fixed obstacle size with each data point being the average of typically 110 shots. Values of $\mathcal{S}_{\text{exp}} \sim 10^{-9}$ were observed over a range of aperture settings. To determine the improvement of $\mathcal{S}_{\text{exp}}$ with the smaller-pixel detector envisaged for the full experiment (nominally reducing the ROI area to 3%), the signal distribution was recorded using the Andor iKon camera. The measurement (Fig. 8) gives a slightly better reduction in background to 1.97%, as a result of the inhomogeneous background distribution shown in Fig. 6.

Correcting the $\mathcal{S}_{\text{exp}}$ measurement for pixel size and T_{A1} we derive shadow factors of $\mathcal{S} < 3 \times 10^{-11}$ from our data for cameras with small pixels for practicable aperture settings.

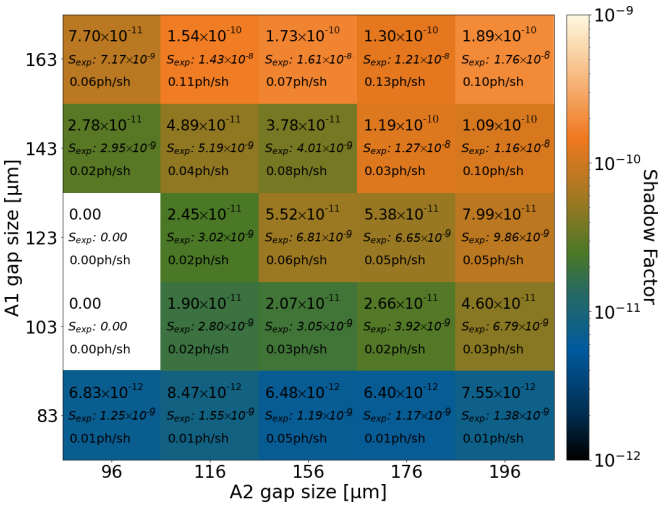

FIG. 7. Results as a function of the aperture sizes A1 and A2. Numbers in each box are the shadow factor $\mathcal{S}$ (top number) for a pixel size 13 μm, which is estimated from the experimentally derived ratio $\mathcal{S}_{\text{exp}}$ measured using the 75 μm pixel Jungfrau detector (middle). Average photon number per shot (bottom) registered in a single 75 μm pixel. The uncertainty in the data is dominated by counting statistics, with each data point corresponding to > 100 shots.

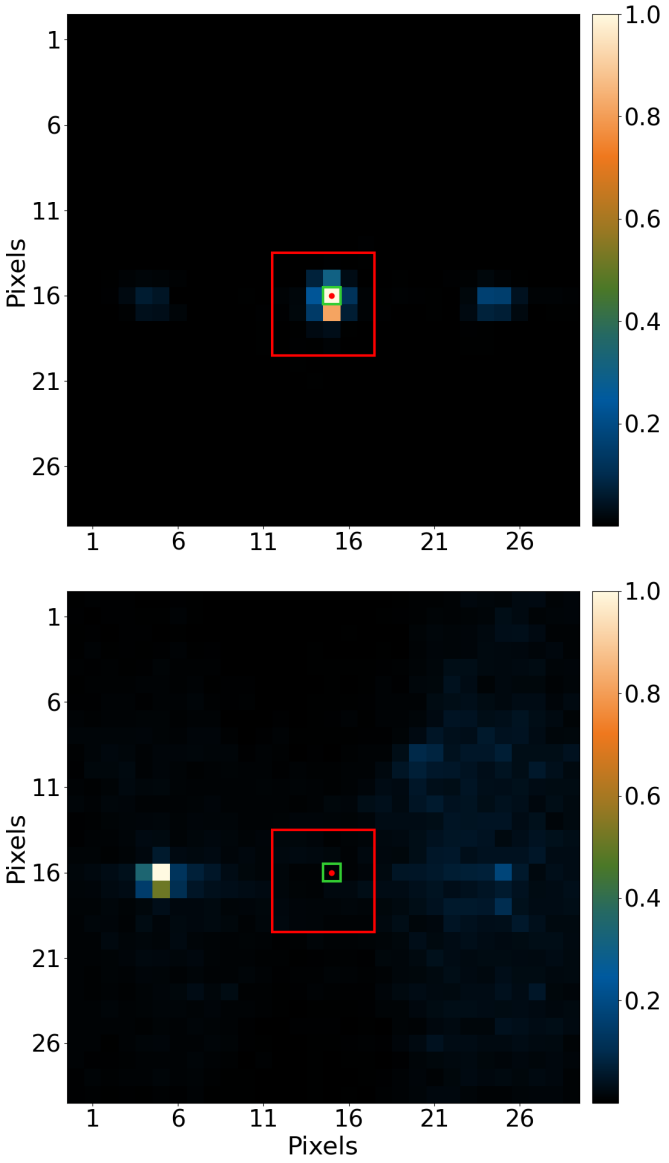

FIG. 8. Focused XFEL beam (above) and dark-field measurement (below) on iKon CCD. The red dot marks our ROI (framed by the lime square) in both images. The red square is the Jungfrau detector pixel size. The ROI on iKon CCD with $13 \times 13\,\mu\text{m}^2$ contains only 1.97 % background compared to the ROI on Jungfrau with $75 \times 75\,\mu\text{m}^2$.

Experimentally derived shadow factors calculated for the planned 13 μm pixel size are shown in Fig. 7 as a function of the aperture width A1, A2 for configuration with obstacle diameters 180 and 160 μm for O1 and O2, respectively. Each each data point is the average of typically 110 shots. The values measured using 75 μm pixels are labeled as $\mathcal{S}_{\text{exp}}$ in the figure.

D. Comparison to simulations

To confirm our understanding of the dark-field setup, the experimental geometry was simulated in a diffraction code based on the *LightPipes* package [18,19]. Figure 9 shows the simulated transverse beam profiles in four critical planes.

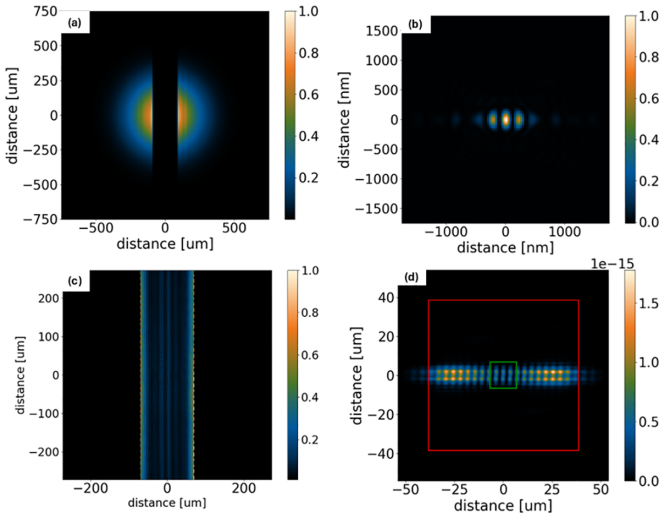

FIG. 9. Simulated transverse profiles of the beam obstructed with beam blocks O1 (diameter 180 μm) and O2 (diameter 160 μm) in four critical planes. (a) Before the first lens, (b) in the focus, (c) after aperture A1 with 140 μm gap, and (d) on the detector. The red square represents the ROI on Jungfrau with $75 \times 75\ \mu m^2$.

These simulations use the experimental parameters used for the data shown in Fig. 7: tungsten wires as obstacles O1 (diameter 180 μm) and O2 (diameter 160 μm), and apertures A1 (gap size 140 μm) and A2 (gap size 100 μm).

The simulations account for diffraction effects and include phase defects characteristic of our lens type as published in the literature [20,21].

The $\mathcal{S}_{\text{exp}}$ shadow factor in the simulations [Fig. 9(d)] $\mathcal{S}_{\text{exp}} = 2.83 \times 10^{-9}$ matches the experimental value 2.95×10^{-9} well (see Fig. 7) for reasonable assumptions regarding the imperfections of the optical elements, particularly lens scattering. We would like to emphasize that the exact numerical value depends sensitively on lens scattering and other imperfections. The simulations are therefore not predictive but rather interpretative of the obtained experimental result. Overall it is found that the simulation results agree very well for the bright features. The object of the simulations here is challenging, in that we are accurately trying to predict areas of the weakest signal. Unsurprisingly, this depends sensitively on simulation details, both numerical and the precise setup of the objects. For example, assuming perfect edges for aperture A1 overestimated the signal level. Adding (estimated) imperfections to A1 aperture edges improved the agreement with the experiment. Nonetheless, the current code has been shown to have sufficiently good agreement to be used to guide setup development.

E. Polarization selection

To determine the coupling parameters a and b, we use a polarization-selective beam splitter made of germanium. The crystal was setup so that each polarization component is reflected by two different symmetry-equivalent crystal planes (440, 404) that enclose an angle of 120°. This method was invented by Baranova and Stepanenko for hexagonal crystals first [22] and further developed for cubic crystals by Wallace, Presura, and Haque [23–25]. Therefore we set the photon energy to $\omega = 8766\,\text{eV}$. The crystals were asymmetrically cut, such that the incoming beam is incident on the crystal surface closer to grazing incidence, but still at a Bragg angle of 45° to the diffracting crystal planes, ensuring increased reflection bandwidth and therefore higher integrated reflectivity.

The polarization purity is defined as the ratio of signal after the polarization analyzer set to measure perpendicular polarization to the signal after the polarization analyzer set to measure parallel polarization. It was determined by rotating the analyzer around the x-ray beam (η-circle) close to the extinction and measuring a rocking curve at each position. The dependence of the integrated intensity of the rocking curves on η is given by Malus's law

$$I(\eta) \propto I_0\left(\sin^2\eta + \mathcal{P}\cos^2\eta\right). \tag{3}$$

The integral reflectivity of the analyzer can be measured with the $\perp$ or $\parallel$ polarized component of the x-ray beam. During the beam time it was figured out that the detector used to measure the $\parallel$ polarized component exhibited a huge spatial inhomogeneity. Therefore, we determine the integral reflectivity of the analyzer crystal with the $\perp$ polarized component as

$$R_{\text{analyser}} = \frac{I(\eta = 0^\circ)}{I_0 \times T_{\text{absorbers}} \times T_{\text{air}} \times \mathcal{P}}, \tag{4}$$

where $I(\eta = 0^\circ)$ represents the measured intensity at the detector in the extinction position, I_0 is the intensity in front of the analyzer, $T_{\text{absorbers}}$ is the transmission of the aluminium absorber foils right in front of the detector, and T_{air} is the transmission of the remaining 1662 mm air in the beam path.

The measured value of $\mathcal{P}$ can be limited by either the polarization of the incoming HXRSS beam, or by the selective power of the crystal. The measurement with an asymmetrical cut crystal with a glancing angle of incidence of ≈24.75° yielded a polarization purity $\mathcal{P} = 6.8 \times 10^{-5}$ and reflectivity $R_{\text{analyzer}} = 25.5\%$ at an estimated energy bandwidth of $\Delta E \approx 0.34\,\text{eV}$. Increasing the asymmetry further to a 331 crystal surface and a resulting glancing angle of ≈13.28° ($\Delta E \approx 0.47\,\text{eV}$) maintained similar levels of polarization purity and reflectivity, with values of $\mathcal{P} = 5.9 \times 10^{-5}$ and $R_{\text{analyzer}} = 21.4\%$. Figure 10 shows the corresponding extinction curve.

Further polarization purity measurements has shown the polarization degradation due to the Be lenses are negligible. The analyzers can effectively improve the shadow quality $\mathcal{S}$ for measurements of the $\perp$-polarized component of the nonlinear quantum vacuum response down to $\mathcal{S}P < 10^{-15}$.

V. DISCUSSION

The above results focus on optimizing the shadow factor. Clearly, the trivial optimum of $\mathcal{S}$ would occur for closed apertures A1, A2. The main constraint on a real-world setup comes from matching the x-ray spatial scale of the x-ray intensity distribution to the size of the high-intensity laser focus. In the limit where the waist of the optical laser $w_{\text{laser}} \gg w_0$, the distribution of the quantum vacuum signal in focus is identical to that of the XFEL beam and therefore the signal on axis is not increased resulting in the quantum vacuum signal being suppressed by essentially the same factor $\mathcal{S}$ as the background. For the matched case we find $w_{\text{laser}} \approx 2w_0$

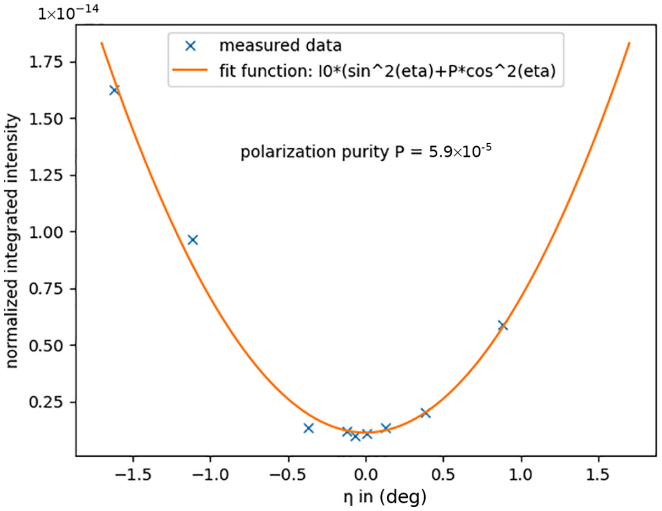

FIG. 10. Extinction curve with Ge-133 analyzer for the determination of the polarization purity $\mathcal{P}$.

resulting in only one dominant peak in the signal distribution in the source point and therefore a peaked distribution of the quantum vacuum signal at the position of A1. These two cases are illustrated in Fig. 11. The combined problem of suppressing the background due to diffraction or scattering while optimizing the quantum vacuum signal is considered for an x-ray photon energy of $\omega = 8766\,\mathrm{eV}$ (FWHM pulse duration 25 fs), optical beam waist $w_{\mathrm{FWHM}} = 1.3\,\mu\mathrm{m}$ (wavelength 800 nm, FWHM pulse duration 30 fs) expected to be attainable with $f/1$ focusing [1,26], a detector acceptance angle due to aperture A1 of $\Theta_{\mathrm{det}} = \Theta_{\mathrm{wire}}/4$. For very small or very large wire diameters the signal trivially goes towards zero. The matching between the w_{laser} and w_0 is calculated by varying the XFEL focusing parameter d/f, where d is the lens beam size and f the CRL focal length. It is seen that the optimal

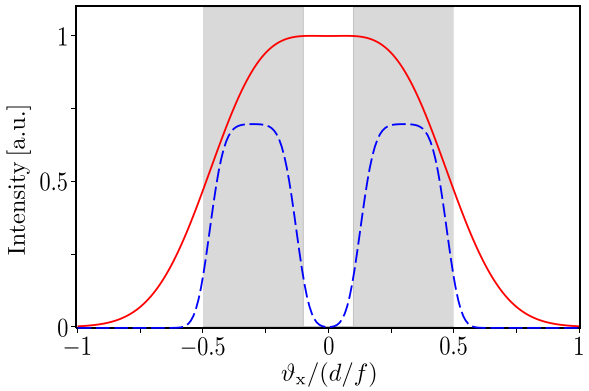

FIG. 11. Distribution of the predicted signal far away from the focus in the direction perpendicular to the obstacle; the blocking fraction is $d_{\mathrm{wire}}/d = 20\%$, and the angle ϑ_x is measured in units of d/f. The gray-shaded areas mark the directions of the bright probe beam and the central white area corresponds to the "shadow" of the obstacle. The solid red curve for $d/f = 140\,\mu\mathrm{rad}$ is matched to the focal spot of the high-intensity laser with $w_{\mathrm{laser}} \approx 2w_0$; cf. Fig. 12. The dashed blue curve for $d/f = 700\,\mu\mathrm{rad}$ illustrates that the signal inherits the "shadow" feature from the probe beam for $w_{\mathrm{laser}} \gg w_0$.

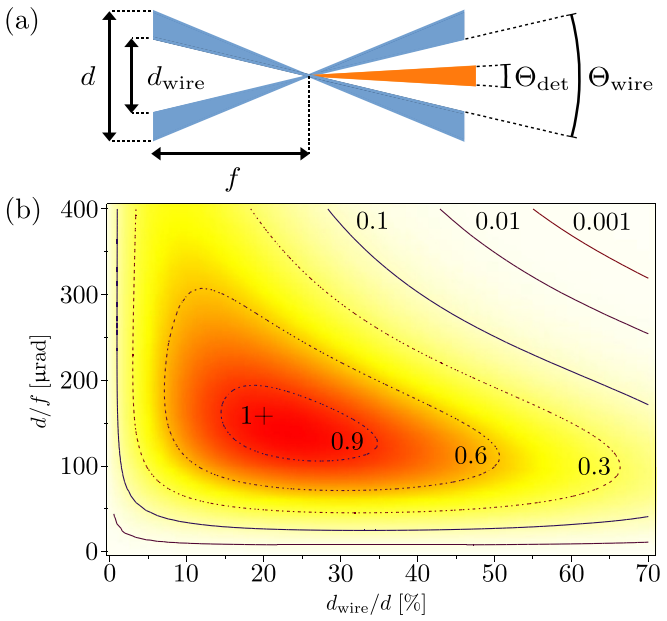

FIG. 12. (a) Sketch of the setting and relevant quantities. (b) Normalized quantum vacuum signal as a function of the blocking fraction d_{wire}/d and the divergence d/f of the x-ray beam; x-ray photon energy $\omega = 8766\,\mathrm{eV}$, optical beam waist $w_{\mathrm{FWHM}} = 1.3\,\mu\mathrm{m}$, and detector acceptance angle $\Theta_{\mathrm{det}} = \Theta_{\mathrm{wire}}/4$. The factors labeling the isocontours indicate the drop of the signal from its maximum value marked by a cross at $d_{\mathrm{wire}}/d = 20\%$ and $d/f = 160\,\mu\mathrm{rad}$.

values lies in the range $d/f = 100 \ldots 200\,\mu\mathrm{rad}$. For larger values, the pump focus is much larger then the probe beam focus, therefore the quantum vacuum signal obtains a spatial distribution nearly identical to that of the probe beam with a central minimum (shadow) and gets blocked on aperture A1.

For the optimal parameters identified in Fig. 12, we obtain

$$N_{\parallel,\perp} \simeq 2.2 \times 10^{-17}\, c_{\parallel,\perp} \left(\frac{W}{1\,\mathrm{J}}\right)^2 N \tag{5}$$

signal photons. Here W is the pulse energy of the optical laser and N is related to the number N_{probe} of focused XFEL photons available for probing the vacuum polarized by the pump pulse as $N = N_{\mathrm{probe}}/(1 - d_{\mathrm{wire}}/d)$. The coefficients $c_{\parallel,\perp}$ depend on a, b and the relative polarization ϕ of pump and probe. For $\phi = \pi/4$ maximizing the polarization-flip signal these simplify to $c_\parallel = (a+b)^2 \simeq 121$ and $c_\perp = (a-b)^2 \simeq 9$, where the numerical values are the leading-order QED predictions; cf. also [8]. The experimental confirmation of a signal N_{sig} in the presence of a background N_{bgr} depends sensitively on the ratio $\mathcal{R} = N_{\mathrm{sig}}/N_{\mathrm{bgr}}$. Achieving a significance of $\#\sigma$ requires the number of successful shots n to fulfill [27]

$$nN_{\mathrm{sig}} > \#^2\, \tfrac{1}{2}[(1+\mathcal{R}^{-1})\ln(1+\mathcal{R}) - 1]^{-1}. \tag{6}$$

The best shadow factor demonstrated above is on the level of $\mathcal{S} = 10^{-11}$. This implies that the background for the $\parallel$ mode consists of $N_{\mathrm{bgr}} = \mathcal{S}N$ photons. Adopting this choice for the $\parallel$ signal in Eq. (5) with the pulse energy in the central Gaussian focus peak of ReLaX given by $W = 4.8\,\mathrm{J}$, we obtain $\mathcal{R} = 6.0 \times 10^{-3}$. Hence, in this case Eq. (6) can be translated into the requirement $n > \#^2\, 2.1 \times 10^{15}/N_{\mathrm{probe}}$.

Accounting for the additional polarization suppression by a factor of $\mathcal{P} = 5.9 \times 10^{-5}$, for the $\perp$ mode we have $N_{\rm bgr} = \mathcal{S}\mathcal{P}N$. For the $\perp$ signal in Eq. (5) with $W = 4.8\,\mathrm{J}$ we thus find $\mathcal{R} = 7.7$, and arrive at the criterion $n > \#^2\, 6.1 \times 10^{13}/N_{\rm probe}$. Despite the higher background in the $\parallel$-channel due to the unavailability of polarization selection, the coupling constants a, b in Eq. (1) can be determined once the significance threshold $\#\sigma$ has been reached in the $\perp$ channel. For $N_\parallel \ll N_{\rm bgr,\parallel}$ the uncertainty is dominated by $N_{\rm bgr,\parallel}$ and given by $\Delta a/a \sim \Delta b/b \sim N_\parallel/\sqrt{N_{\rm bgr,\parallel}}$.

The number of photons N_0 contained in the central Airy peak of $1/e^2$ width is related to the total number of photons N in the focus of the unobstructed beam as $N_0/N = 1 - J_0^2[2\sqrt{2(1-e^{-1})}] - J_1^2[2\sqrt{2(1-e^{-1})}] = 69\%$. Hence, the value of N_0 in the present proof-of-principle experiment extracted in Sec. IV implies $N_{\rm probe} = 7.57 \times 10^{10}$ for an optimal blocking of $d_{\rm wire}/d = 20\%$ and current EuXFEL performance. With this value the above requirements on the numbers of successful shots become $n > \#^2\, 2.8 \times 10^4$ for the $\parallel$ signal and $n > \#^2\, 8.0 \times 10^2$ for the $\perp$ signal. We emphasize that these conditions could be substantially improved by increasing the pulse energy of the optical laser. For instance, increasing the laser pulse energy by a factor of ten would decrease the threshold on n for the $\parallel$ signal by a factor of $\approx 8.4 \times 10^3$ and that for the $\perp$ signal by a factor of $\approx 3.9 \times 10^2$.

VI. CONCLUSION AND OUTLOOK

The dark-field concept is a highly promising variant on the road to direct experimental studies of the optical response of the quantum vacuum. The concept promises a detectable signal level despite the large number of probe photons that can contribute to unwanted background and the small cross sections. The dark-field approach allows the determination of the fundamental constants governing nonlinear quantum vacuum interactions for measurements of both parallel and perpendicularly polarized signal components and, at reduced experimental demands, a measurement of the perpendicularly polarized component only. The experimental results show that sufficiently good background suppression can be achieved in a beamline with real-world optical components, opening the path to measuring the nonlinear response of the vacuum.

ACKNOWLEDGMENTS

We acknowledge the European XFEL in Schenefeld, Germany, for provision of x-ray free-electron laser beamtime under the HIBEF priority access route at the Scientific Instrument HED (High Energy Density Science) under Proposals No. 5438 and 6436. We are grateful for assistance and dedication of the XFEL and HIBEF staff that enabled this experiment. This work has been funded by the Deutsche Forschungsgemeinschaft (DFG, German Research Foundation) under Grants No. 392856280, No. 416607684, No. 416702141, and No. 416708866 within the Research Unit FOR2783/2. We are grateful to all members of the BIREF@HIBEF Collaboration for interest and support.

DATA AVAILABILITY

The data that support the findings of this article are openly available [28,29]; embargo periods may apply.

[1] N. Ahmadiniaz *et al.*, Letter of intent: Towards a vacuum birefringence experiment at the Helmholtz International Beamline for Extreme Fields, High Power Laser Sci. Eng. **13**, e7 (2025).

[2] A. Fedotov, A. Ilderton, F. Karbstein, B. King, D. Seipt, H. Taya, and G. Torgrimsson, Advances in QED with intense background fields, Phys. Rep. **1010**, 1 (2023).

[3] H. Euler and B. Kockel, The scattering of light by light in Dirac's theory, Naturwissenschaften **23**, 15, 246 (1935).

[4] W. Heisenberg and H. Euler, Consequences of Dirac's theory of positrons, Z. Phys. **98**, 714 (1936).

[5] J. Peatross, J. L. Chaloupka, and D. D. Meyerhofer, High-order harmonic generation with an annular laser beam, Opt. Lett. **19** 942 (1994).

[6] M. Zepf *et al.*, Role of the plasma scale length in the harmonic generation from solid targets, Phys. Rev. E **58**, R5253 (1998).

[7] F. Karbstein and E. A. Mosman, Enhancing quantum vacuum signatures with tailored laser beams, Phys. Rev. D **101**, 113002 (2020).

[8] F. Karbstein, D. Ullmann, E. A. Mosman, and M. Zepf, Direct accessibility of the fundamental constants governing light-by-light scattering, Phys. Rev. Lett. **129**, 061802 (2022).

[9] U. Zastrau *et al.*, The high energy density scientific instrument at the European XFEL, J. Synchrotron Radiat. **28**, 1393 (2021).

[10] I. Lyatun *et al.*, Impact of beryllium microstructure on the imaging and optical properties of x-ray refractive lenses, J. Synchrotron Radiat. **27**, 44 (2020).

[11] S. Liu, W. Decking, V. Kocharyan, E. Saldin, S. Serkez, R. Shayduk, H. Sinn, and G. Geloni, Preparing for high-repetition rate hard x-ray self-seeding at the European X-ray free electron laser: Challenges and opportunities, Phys. Rev. Accel. Beams **22**, 060704 (2019).

[12] N. Kujala *et al.*, Hard x-ray single-shot spectrometer at the European X-ray free electron laser, Rev. Sci. Instrum. **91**, 103101 (2020).

[13] J. Chalupský *et al.*, Fluence scan: An unexplored property of a laser beam, Opt. Express **21**, 22, 26363 (2013).

[14] G. Mercurio *et al.*, Real-time spatial characterization of micrometer-sized x-ray free-electron laser beams focused by bendable mirrors, Opt. Express **30**, 20980 (2022).

[15] F. Karbstein, Quantum vacuum nonlinearities in strong electromagnetic fields, habilitation thesis, Faculty of Physics and Astronomy, Friedrich-Schiller-Universität Jena, 2024, https://www.db-thueringen.de/receive/dbt_mods_00059618.

[16] F. Karbstein, E. A. Mosman, and M. Zepf (unpublished).

[17] M. Sikorski *et al.*, First operation of the Jngfrau detector in 16-memory cell mode at European XFEL, Front. Phys. **11**, 1303247 (2023).

[18] G. Vdovin, H. van Brug, and F. van Goor, LightPipes: Software for education in coherent optics, Proc. SPIE **3190**, 82 (1997).

[19] G. Vdovin and F. van Goor, LightPipes for Python 2.1.5, https://opticspy.github.io/lightpipes/.

[20] F. Seiboth *et al.*, Nanofocusing with aberration-corrected rotationally parabolic refractive x-ray lenses, J. Synchrotron Rad. **25**, 108 (2018).

[21] R. Celestre *et al.*, Modelling phase imperfections in compound refractive lenses, J. Synchrotron Rad. **27**, 305 (2020).

[22] E. O. Baranova and M. M. Stepanenko, A novel x-ray polarimeter based on hexagonal crystal for application to thermonuclear fusion experiments, Plasma Phys. Control. Fusion **45**, 1113 (2003).

[23] M. S. Wallace *et al.*, Cubic crystals in an x-ray-splitting geometry, Rev. Sci. Instrum. **91**, 023105 (2020).

[24] M. S. Wallace *et al.*, Polarisation splitting with cubic crystals evaluated with synchrotron radiation, Rev. Sci. Instrum. **92**, 103101 (2021).

[25] R. Presura *et al.*, Extension of single-crystal x-ray spectropolarimetry with cubic crystals beyond perfect-splitting geometries, Rev. Sci. Instrum. **92**, 073102 (2021).

[26] A. Laso Garcia *et al.*, ReLaX: The Helmholtz international beamline for extreme fields high-intensity short-pulse laser driver for relativistic laser–matter interaction and strong-field science using the high energy density instrument at the european X-ray free electron laser facility, High Power Laser Sci. Eng. **9**, e59 (2021).

[27] G. Cowan, K. Cranmer, E. Gross, and O. Vitells, Asymptotic formulae for likelihood-based tests of new physics, Eur. Phys. J. C **71**, 1554 (2011); **73**(E), 2501 (2013).

[28] Data publication, HIBEF PA—Towards quantum vacuum birefringence using an x-ray dark-field technique, https://in.xfel.eu/metadata/doi/10.22003/XFEL.EU-DATA-005438-00.

[29] Data publication, HIBEF PA—Next step towards vacuum birefringence using an x-ray dark-field technique, https://in.xfel.eu/metadata/doi/10.22003/XFEL.EU-DATA-006436-00.